





## Article

# Deciphering the Interplay between Binders and Electrolytes on the Performance of $\text{Li}_4\text{Ti}_5\text{O}_{12}$ Electrodes for Li-Ion Batteries

Francesca De Giorgio <sup>1,2,3,\*</sup> , Mattia Gaboardi <sup>4</sup> , Lara Gigli <sup>4</sup>, Sergio Brutti <sup>3,5,6,\*</sup>  and Catia Arbizzani <sup>2,3</sup> 

- <sup>1</sup> Consiglio Nazionale delle Ricerche, Istituto per lo Studio dei Materiali Nanostrutturati (CNR-ISMN), Via P. Gobetti 101, 40129 Bologna, Italy
  - <sup>2</sup> Department of Chemistry “Giacomo Ciamician”, Alma Mater Studiorum—Università di Bologna, Via F. Selmi 2, 40126 Bologna, Italy; catia.arbizzani@unibo.it
  - <sup>3</sup> GISEL—National Centre of Reference for Electrochemical Energy Storage Systems, INSTM, Via G. Giusti 9, 50121 Firenze, Italy
  - <sup>4</sup> Elettra-Sincrotrone Trieste S.C.p.A., s.s. 14—km 163.5 in Area Science Park, Basovizza, 34149 Trieste, Italy; mattia.gaboardi@elettra.eu (M.G.); lara.gigli@elettra.eu (L.G.)
  - <sup>5</sup> Department of Chemistry, University of Rome “La Sapienza”, P. A. Moro 5, 00185 Rome, Italy
  - <sup>6</sup> Institute for Complex System, National Research Council (ISC-CNR), UOS Sapienza, Via dei Taurini, 00185 Roma, Italy
- \* Correspondence: francesca.degiorgio@cnr.it (F.D.G.); sergio.brutti@uniroma1.it (S.B.)

**Abstract:** Lithium titanium oxide ( $\text{Li}_4\text{Ti}_5\text{O}_{12}$ , LTO) is an attractive negative electrode for the development of safe—next-generation—lithium-ion batteries (LIBs). LTO can find specific applications complementary to existing alternatives for LIBs thanks to its good rate capability at high C-rates, fast lithium intercalation, and high cycling stability. Furthermore, LIBs featuring LTO electrodes are inherently safer owing to the LTO’s operating potential of 1.55 V vs.  $\text{Li}^+/\text{Li}$  where the commonly used organic-based electrolytes are thermodynamically stable. Herein, we report the combined use of water-soluble sodium alginate (SA) binder and lithium bis(trifluoromethanesulfonyl)imide (LiTFSI)-tetraglyme (1m-T) electrolyte and we demonstrate the improvement of the electrochemical performance of LTO-based electrodes with respect to those operating in conventional electrolyte 1 M  $\text{LiPF}_6$ -ethylene carbonate: dimethyl carbonate (LP30). We also tackle the analysis of the impact of combining the binder/electrolyte on the long-term cycling performance of LTO electrodes featuring SA or conventional polyvinylidene fluoride (PVdF) as binders. Therefore, to assess the impact of the combination of binder/electrolyte on performance, we performed post-mortem characterization by ex situ synchrotron diffraction experiments of LTO electrodes after cycling in LP30 and 1m-T electrolytes.

**Keywords:**  $\text{Li}_4\text{Ti}_5\text{O}_{12}$ ; LTO; synchrotron X-ray diffraction (XRD); sodium alginate binder; tetraglyme-based electrolyte



**Citation:** De Giorgio, F.; Gaboardi, M.; Gigli, L.; Brutti, S.; Arbizzani, C. Deciphering the Interplay between Binders and Electrolytes on the Performance of  $\text{Li}_4\text{Ti}_5\text{O}_{12}$  Electrodes for Li-Ion Batteries. *Energies* **2022**, *15*, 4182. <https://doi.org/10.3390/en15124182>

Academic Editors: Carlos Miguel Costa and Muhammad Aziz

Received: 2 May 2022

Accepted: 3 June 2022

Published: 7 June 2022

**Publisher’s Note:** MDPI stays neutral with regard to jurisdictional claims in published maps and institutional affiliations.



**Copyright:** © 2022 by the authors. Licensee MDPI, Basel, Switzerland. This article is an open access article distributed under the terms and conditions of the Creative Commons Attribution (CC BY) license (<https://creativecommons.org/licenses/by/4.0/>).

## 1. Introduction

The exponential growth of the electric transport sector will lead to an increase in electric vehicles (EVs) from around 5% of global car sales to more than 60% by 2030 [1]. The electrification of transport is the main driver for the dramatic battery demand increase with a global market forecast for lithium-ion batteries (LIBs) that could reach up to 4 TWh by 2040 compared to 78 GWh today [2]. Batteries are the key near-term enabling technology to decarbonize road transportation and support the transition to a renewable power system, thus achieving the targets of the Paris Agreement and UN Sustainable Development Goals [3].

Regardless of the application (i.e., EVs and grid-scale storage), the huge battery demand and the commitment of Europe to achieve a climate-neutral society by 2050 calls for the development of the next generation of lithium-ion and lithium batteries featuring higher performances than current LIBs in terms of safety, cost-efficiency, environment and social sustainability, energy, and power density [4–6].

Different strategies aim at addressing such challenges either by focusing on the improvement of battery cell components—i.e., anode and cathode materials, binders, electrolytes, and separators—or by developing new battery chemistries [7–9].

In addition to the graphite anode, the spinel-structured lithium titanium oxide ( $\text{Li}_4\text{Ti}_5\text{O}_{12}$ , LTO) is one of the most attractive anode materials for LIBs, thanks to its good rate capability at high C-rates, fast lithium intercalation, and high cycling stability [5,10–12]. Björklunde et al. demonstrated that  $\text{LiNi}_{1/3}\text{Co}_{1/3}\text{Mn}_{1/3}\text{O}_2$  (NMC)-LTO and NMC-graphite cells show a small fading over 200 cycles in carbonate-based electrolyte [13].

Despite low theoretical specific capacity ( $175 \text{ mAh g}^{-1}_{\text{LTO}}$  vs.  $372 \text{ mAh g}^{-1}_{\text{graphite}}$ ) and lower energy density provided in full-cell configurations than graphite-based cells, LTO features an operating potential of ca. 1.55 V vs.  $\text{Li}^+/\text{Li}$  where the commonly used organic-based electrolytes are thermodynamically stable, mitigating the formation of solid electrolyte interphase (SEI) over cycling. Hence, the safety concerns related to lithium plating and = consequent dendrite formation are prevented. As “zero-strain material”, LTO does not suffer from volume change upon the two-phase (spinel to rock-salt) electrochemical process of  $\text{Li}^+$  insertion/de-insertion; thus, it is extremely suitable to develop high-power batteries for applications such as grid stabilization, electrically driven roll-on/roll-off ferries, and near-term EVs [14–17].

The matching of LTO anode with high-operating potential cathodes such as  $\text{LiNi}_{0.5}\text{Mn}_{1.5}\text{O}_4$  ( $>4.70\text{--}4.75 \text{ V}$  vs.  $\text{Li}^+/\text{Li}$ ) might allow full cells with higher overall operating voltage and specific energy than those with conventional cathodes such as  $\text{LiFePO}_4$  [18–21].

Despite the above advantages, LTO suffers from low electrical conductivity ( $10^{-13} \text{ S cm}^{-1}$ ) and Li-ion diffusion coefficient ( $10^{-9}\text{--}10^{-13} \text{ cm}^2 \text{ s}^{-1}$ ) and severe gassing phenomenon occurring during charge/discharge cycles and storage, which leads to severe swelling and safety issues. Approaches to improve rate performance and specific capacity of LTO electrodes include surface modification (e.g., carbon coating) [22], particle size reduction to the sub-micron and nanometer-scale [23,24], novel solid-phase synthesis [25], development of ultrafine nanocrystals and novel composite architectures [26], ion doping (e.g., Co, Mn, Cr, and Ni) [27–30], and the use of suitable binders [31–34].

The gassing phenomenon is the major concern of LTO-based cells and it is mainly due to the electrode/electrolyte interface reactions that generate  $\text{H}_2$ ,  $\text{CO}_2$ ,  $\text{CO}$ , and alkanes/olefins derivatives arising from the decomposition of organic electrolytes as detected by operando investigations with online electrochemical mass spectrometry (OEMS) [35,36]. The decomposition of electrolyte solvents and salts, which is accelerated at elevated operating temperatures, is also responsible for the gas evolution, as well as water contamination from electrolyte or residual hydroxyl groups on LTO's surface from electrode manufacturing [36–40]. Several strategies to mitigate the gassing behavior were proposed. The use of an ultrathin carbon coating layer of LTO was demonstrated to effectively suppress the gassing behavior, resulting in enhanced rate capability [41]. Film-forming electrolyte additives such as sulfonyl imides and borates also mitigate gas evolution, passivating the LTO's surface [42,43].

In our previous work [44], we exploited for the first time the combined use of an eco-friendly, water-processable sodium alginate (SA) binder and glyme-based electrolyte as an effective strategy to improve the electrode/electrolyte interface in LTO-based cells featuring different percentage of active material (80, 87, and 90 wt.%). The SA binder and 1 molal (mol/kg) lithium bis(trifluoromethanesulfonyl)imide (LiTFSI)–tetraglyme (1m-T) electrolyte were used as alternative to conventional polyvinylidene fluoride (PVdF) binder and 1 M  $\text{LiPF}_6$ –ethylene carbonate: dimethyl carbonate (LP30) electrolyte, which are the most commonly used in commercial LIBs. LiTFSI salt was used to replace  $\text{LiPF}_6$  owing to its higher stability [45], and it was reported that LiTFSI-glyme-based electrolytes have beneficial effects in enhancing the rate capability of LTO// $\text{LiFePO}_4$  cells with electrodes containing a PVdF binder [46]. Moreover, compared to carbonate-based electrolyte, glymes, and particularly those with longer chain lengths such as tetraglyme, display higher safety,

lower flammability and flash point, and less relevant toxicity, apart from possible fertility issues expected for glymes featuring lower chain lengths [47].

In Ref. [44], we demonstrated that LTO-based electrodes tested in 1m-T electrolyte show higher electrochemical performance than those in LP30. We investigated three different electrode formulations based on LTO: carbon black: SA, i.e., 90:7:3, 87:10:3, and 80:10:10; the latter was used for comparisons with the benchmark formulation featuring the PVdF binder (80:10:10). Thanks to a good balance between high active material percentage, good electronic conductivity, and good carbon-to-binder ratio, we proved that electrodes with 87% LTO and 3% SA binder show the best electrochemical performance. Indeed, they displayed a rate capability comparable to that of conventional electrode formulation with 80% LTO and PVdF binder operating in LP30, and they showed excellent cycling stability over 600 charge/discharge cycles at 1C in both 1m-T and LP30 electrolytes. Electrochemical impedance spectroscopy (EIS) analysis carried out before and after 600 cycles revealed that the total impedance increase in LTO-SA electrode in 1m-T is lower than in LP30, thanks to a thin surface layer that is formed in the presence of 1m-T and remains stable over cycling.

Based on our previous findings, herein we tackle for the first time, to the best of our knowledge, a comprehensive post-mortem characterization by ex situ synchrotron X-ray powder diffraction (XRD) on LTO electrodes after long-term cycling in LP30 and 1m-T to assess the impact of the combination of binder/electrolyte on performance. Pristine and cycled LTO electrodes with two different electrode formulations were analyzed. We compare the best performing LTO-SA electrode formulation, i.e., 87% LTO active material: 10% conductive carbon: 3% SA binder with the best conventional LTO-PVdF electrode formulation featuring 80% LTO and 10% PVdF. The ex situ XRD experiments were performed on fully de-lithiated  $\text{Li}_4\text{Ti}_5\text{O}_{12}$  (discharged state) samples since they are more thermally and chemically stable over time compared to the lithiated  $\text{Li}_7\text{Ti}_5\text{O}_{12}$  ones. Indeed, in fully lithiated LTO, spontaneous  $\text{Ti}^{3+}$  oxidation can occur in the atmosphere, thus leading to possible degradation during the XRD measurements.

## 2. Materials and Methods

### 2.1. Electrode Preparation and Electrochemical Characterization

LTO-based electrodes containing sodium alginate (SA, Sigma-Aldrich, Milano, Italy) or polyvinylidene difluoride (PVdF, Kynar<sup>®</sup> LBG, Arkema, Colombes Cedex, France) binders were prepared according to the procedure described in our previous work [44] by using commercial lithium titanium oxide powder (Toda Kogyo Corp., Minami-ku, Hiroshima, Japan). The water-processed LTO-SA consisted of 87 wt% active material, 10 wt% C-energy Super C45 (C45, Imerys Graphite & Carbon, Bironico, Switzerland) conducting carbon, and 3 wt% SA, and the LTO-PVdF ones consisted of 80 wt% LTO, 10 wt% C65, and 10 wt% PVdF.

The slurries were deposited on a carbon-coated Al foil current collector by using a lab-scale mini coating machine (MC 20, Hohsen Corp., Chuo-ku, Osaka, Japan) and pre-dried at 60 °C overnight in air. Disk electrodes of 0.636 cm<sup>2</sup> (LTO-SA) and 0.785 cm<sup>2</sup> (LTO-PVdF) featuring active material mass loading in the range of 2–5 mg cm<sup>-2</sup> were punched and dried at 110 °C under dynamic vacuum in a Büchi glass oven for 12 h before use.

The electrochemical tests were carried out with Biologic VSP multichannel potentiostat/galvanostat and MTI Corp battery tester instruments at 30 °C in two-electrode mode by using Teflon<sup>®</sup> T-shaped BOLA (Bohlender GmbH, Grünsfeld, Germany) cells without an electrolyte reservoir. LTO-SA and LTO-PVdF were used as working electrodes, Li metal was used as the counter-electrode, and Whatman GF/D glass fiber (GE Healthcare Ltd., Little Chalfont, UK) soaked with 50 µL electrolyte was used as a separator. The electrolytes were 1 M  $\text{LiPF}_6$ -ethylene carbonate (EC): dimethyl carbonate (DMC) 1:1 *w/w* (Selectilyte LP30, BASF, Ludwigshafen, Germany) and 1 molal (mol/kg) Li bis(trifluoromethane) sulfonimide ( $\text{LiTFSI}$ , ≥99.0% Sigma-Aldrich, Merck KGaA, Darmstadt, Germany) in tetraethylene glycol dimethyl ether (TEGDME, ≥99% Sigma-Aldrich, Merck KGaA, Darmstadt, Germany), hereinafter called LP30 and 1m-T, respectively.

After assembly, the cells were kept for 3 h in open circuit potential at 30 °C. The electrochemical tests between 1.0 V and 2.2 V consisted of five galvanostatic charge/discharge cycles at C/3 (conditioning cycles), followed by long-term cycling, i.e., 50, 100, 250, and 500 cycles at 1C. Charge and discharge refer to lithiation and de-lithiation processes, respectively. As the end conditions of each charging and discharging step, the cut-off voltages of 1.0 and 2.2 V and time duration of 3 h (for cycles at C/3) and 1 h (for cycles at 1C) were set. The C-rates were calculated on LTO's theoretical specific capacity of 175 mAh g<sup>-1</sup><sub>LTO</sub>. Table 1 shows the LTO-based electrodes tested at the ELETTRA synchrotron MCX beamline. SAL and SAT refer to LTO-SA electrodes tested in LP30 and 1m-T electrolytes, respectively; PVL and PVT refer to LTO-PVdF electrodes tested in LP30 and 1m-T. The critical samples have been replicated in order to consolidate the experimental outcomes.

**Table 1.** LTO-based electrodes tested at ELETTRA synchrotron MCX beamline and refinement convergences.

LTO-SA Code	Electrolyte	Rietveld Refinement Convergences wRp, GoF	LTO-PVdF Code	Electrolyte	Rietveld Refinement Convergences wRp, GoF
SA_1	Pristine electrode	4.8%, 1.5	PV_1	Pristine electrode	5.2%, 1.1
SAL_1	LP30	5.3%, 1.2	PVL_1	LP30	5.9%, 1.8
SAL_2	LP30	5.8%, 1.3	PVL_2	LP30	5.4%, 1.6
SAL_3	LP30	4.8%, 1.4	PVL_3	LP30	5.2%, 1.6
SAL_4	LP30	5.1%, 1.1	PVL_4	LP30	6.8%, 1.0
SAT_5	1m-T	5.1%, 1.3	PVT_5	1m-T	6.4%, 1.5
SAT_6	1m-T	5.3%, 1.3	PVT_6	1m-T	6.9%, 1.0
SAT_7	1m-T	6.2%, 0.8	PVT_7	1m-T	5.5%, 1.7
SAT_8	1m-T	6.4%, 1.2	PVT_8	1m-T	6.9%, 1.8
			PVT_9	1m-T	5.3%, 1.6

## 2.2. X-ray Diffraction Experiments

The XRD experiments were carried out at the ELETTRA synchrotron radiation source (MCX beamline [48], using the 4 circle diffractometer in theta-2theta geometry). The diffraction patterns have been recorded in the 13–71 2θ degree range using an energy of 10 keV (wavelength 1.2398 Å) with a 2θ step of 0.01°. The diffraction pattern of a flat plate containing standard crystalline silicon powder was also recorded at the same experimental conditions as standard.

The XRD experiments were carried out on pristine and cycled LTO-SA and LTO-PVdF electrodes (Table 1) with a size of 9 mm (LTO-SA) and 10 mm (LTO-PVdF) diameter. At the end of the prolonged galvanostatic discharge/charge cycles, the Li/LTO half-cells were disassembled in an Ar-filled glove box, and the electrodes were recovered, rinsed in dried DMC (electrodes tested in LP30) or tetrahydrofuran (electrodes tested in 1m-T) and then placed on an Al flat plate XRD sample holder and sealed with Kapton tape (Figure 1).



**Figure 1.** Sample holder (Al flat plate) with the electrode specimen (dark disk at the center) sealed with Kapton tape in an Ar-filled glove box.

The XRD pattern of LTO commercial powder has been recorded in the 10–90  $2\theta$  degree range with a PANalytical X'Pert PRO powder diffractometer equipped with a X'Celerator detector (CuK $\alpha$  radiation, 40 mA, 40 kV).

Structure refinement has been performed via the Rietveld method using the GSAS-II software suite [49]. The structural model adopted is the Li<sub>4</sub>Ti<sub>5</sub>O<sub>12</sub> spinel lattice as summarized in Table 2, and refinement convergences are reported in the Table 1. Structural data have been obtained from Ref. [50].

**Table 2.** Crystal structure parameters of the LTO spinel lattice (space group Fd-3m, number 227 origin choice 1, and DW = Debye Waller factor).

Cubic Cell Parameter	Atoms	Wyckoff Position	Atomic Coordinates x, y, z	DW/10 <sup>-2</sup> A <sup>2</sup>	Occupancies
$a = 8.359 \pm 0.001 \text{ \AA}$	Li	8a	0 0 0	1	1.0
	Li	16d	$1/2 \ 1/2 \ 1/2$	1	$1/6$
	Ti	16d	$1/2 \ 1/2 \ 1/2$	1	$5/6$
	O	32e	0.261 0.261 0.261	1	1.0

In addition to background and arbitrary intensity, the following parameters were refined: the cubic lattice parameter,  $a$ ; the crystallite size,  $D$ ; the microstrain,  $\sigma$ ; Debye–Waller factors, DW. Only one major constraint has been adopted by assuming that DW factors were equivalent for all atoms. The theoretical reconstructions of the diffraction pattern have been, therefore, matched with the experimental one by minimizing the chi square function. The quality of the refinement has been evaluated by calculating the so-called  $wRp$  and the Gof factors [51].

### 3. Results and Discussion

Figure 2 shows the XRD pattern of the pristine LTO (indexed to the expected space group Fd-3m): We used commercial powder for the manufacture of LTO-SA and LTO-PVdF electrodes. During lithiation, i.e., the charge process, three Li<sup>+</sup> ions are inserted into LTO lattice, leading to a phase transition from the Li<sub>4</sub>Ti<sub>5</sub>O<sub>12</sub> spinel structure to the Li<sub>7</sub>Ti<sub>5</sub>O<sub>12</sub> rock-salt structure, according to the following reaction [52,53].

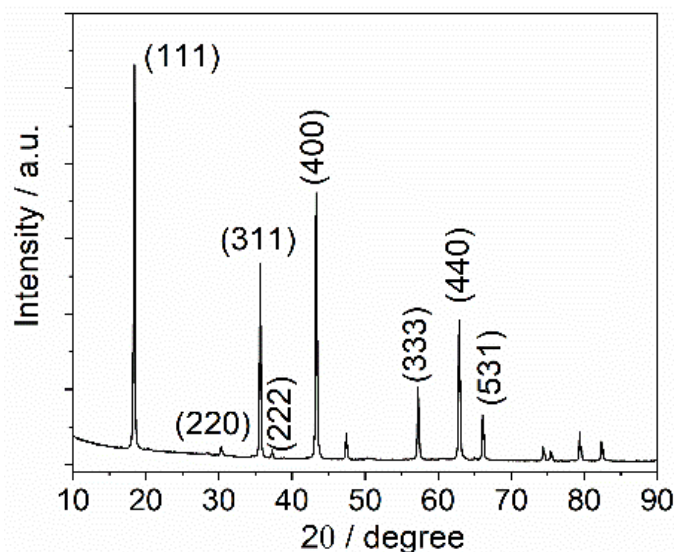
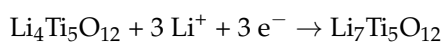


**Figure 2.** XRD pattern of LTO commercial powder.

In terms of crystallographic changes, the intercalation of lithium occurs through a single-phase incorporation of lithium ions [54,55], occurring in parallel to the migration of the already existing lithium ions in the structure from the tetrahedral-8a site to the octahedral-16c site. This intercalation reaction occurs through an extraordinarily stable plateau and it is “zero-strain” as the lattice is marginally altered upon lithiation [52]. This peculiar structural feature allows for an extraordinary reversibility of the intercalation reaction from/into the  $\text{Li}_4\text{Ti}_5\text{O}_{12}$  spinel structure.

As demonstrated by us in Ref. [44], here it is confirmed that the long-term stability performance of LTO-SA electrodes over 500 cycles is higher than that of LTO-PVdF both in 1m-T and LP30 (Figure 3). LTO-PVdF shows very poor cycling performance in both electrolytes and suffers from side reactions mainly over de-lithiation process. Although LTO-SA shows slightly lower specific capacity at 1C during the de-lithiation process (Table 3) than LTO-PVdF (Table 4), the capacity retention between the last and the first cycle at 1C is notably higher than LTO-PVdF. Indeed, after 500 cycles at 1C, LTO-SA features a capacity retention of 57% and 76% in LP30 and 1m-T, respectively, against 16% and 2% of LTO-PVdF.

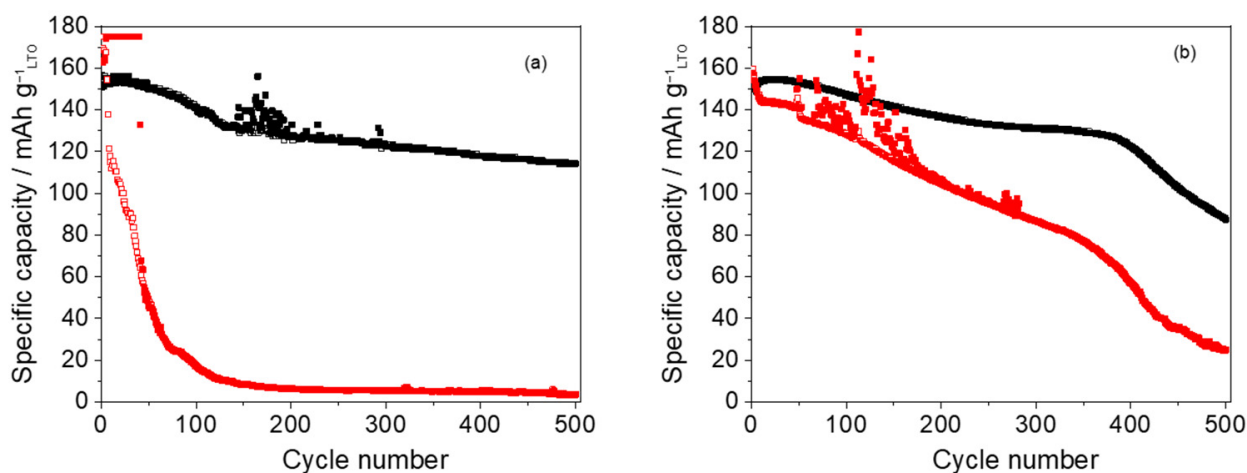


**Figure 3.** Specific capacity delivered during the lithiation (empty symbol) and de-lithiation (full symbol) processes of LTO-SA (black symbol) and LTO-PVdF (red symbol) over 500 cycles at 1C in (a) 1m-T and (b) LP30.

**Table 3.** Specific capacity ( $\text{mAh g}^{-1}_{\text{LTO}}$ ) during de-lithiation process at the first and last cycle at 1C and capacity retention of LTO-SA tested in LP30 and 1m-T.

LTO-SA Code	Electrolyte	N. Cycles at 1C	Specific Capacity	Specific Capacity	Capacity
			1st Cycle *	Last Cycle *	Retention **
			$\text{mAh g}^{-1}_{\text{LTO}}$		%
SAL_1	LP30	500	153	87	57
SAL_2	LP30	250	152	135	89
SAL_3	LP30	100	156	131	84
SAL_4	LP30	50	152	110	72
SAT_5	1m-T	500	151	114	75
SAT_6	1m-T	250	153	102	67
SAT_7	1m-T	100	155	147	95
SAT_8	1m-T	50	158	157	99

\* Discharge specific capacity at 1C. \*\* Capacity retention (%) between the last and the first cycle at 1C.

**Table 4.** Specific capacity ( $\text{mAh g}^{-1}_{\text{LTO}}$ ) during de-lithiation process at the first and last cycle at 1C and capacity retention of LTO-PVdF tested in LP30 and 1m-T.

LTO-PVdF Code	Electrolyte	N. Cycles at 1C	Specific Capacity	Specific Capacity	Capacity
			1st Cycle *	Last Cycle *	Retention **
			$\text{mAh g}^{-1}_{\text{LTO}}$		%
PVL_1	LP30	500	158	25	16
PVL_2	LP30	250	163	7	4
PVL_3	LP30	250	154	85	55
PVL_4	LP30	100	168	228	136 ***
PVT_5	1m-T	500	163	4	2
PVT_6	1m-T	250	156	4	3
PVT_7	1m-T	250	113	5	4
PVT_8	1m-T	100	162	30	19
PVT_9	1m-T	50	153	175	114 ***

\* Specific capacity at 1C. \*\* Capacity retention (%) between the last and the first cycle at 1C. \*\*\* Side reactions occurred over the de-lithiation process.

The ex situ scanning electron microscopy (SEM) analyses that we reported in Ref. [44] revealed that, while LTO-SA still displays a compact and homogeneous structure after cycling in LP30, the LTO-PVdF electrode's surface is fully covered by a passivation layer caused by the swollen binder after electrochemical tests in LP30. On the other hand, SEM images of the cycled LTO-based electrodes in 1m-T showed rather compact, homogeneous structure and a small passivation layer on both LTO-SA and LTO-PVdF surfaces, suggesting that the side reactions at the electrode/electrolyte interface do not greatly affect the electrode's morphology in 1m-T, irrespective of the binder. Undesired side-reactions at the electrode/electrolyte interface are then more facilitated in LP30 than in 1m-T [44].

Therefore, the ex situ XRD study carried out on pristine and cycled LTO electrodes is aimed at investigating how the binder and electrolyte can affect the electrode's structure changes upon long-term cycling. The electrodes have been tested after long-term cycles at different cycling times, since the side reactions proceed over cycling, and phase and electrode morphology changes may be appreciated only after long-term cycling in LP30 and 1m-T electrolytes.

Twenty XRD patterns were collected on pristine and cycled LTO electrodes in the discharged (de-lithiated) state. Figure 4 shows a summary of the XRD patterns collected at ELETTRA.

The first qualitative output suggests that the LTO spinel structure is maintained upon cycling in both electrolytes despite the use of different binders. No anatase  $\text{TiO}_2$  peaks are present, thus highlighting that the interfacial reactions at the LTO–electrolyte interface do not promote remarkable structure changes upon cycling. Spurious additional diffraction peaks not indexed by the spinel lattice have been observed. All strong unindexed reflections were easily assigned to aluminum. Two inevitable sources of aluminum are present in the samples: the metal foil below the casted electrode as well as the XRD sample holder. Both of these sources have preferential orientation. Furthermore, the surface of electrodes, especially after prolonged cycling, can be easily damaged during the “cell de-assembling/washing/drying/sealing” procedure, thus exposing uncoated aluminum areas. In addition to aluminum, the absence of additional indexed diffraction features allows us to exclude the precipitation of other  $\text{TiO}_2$ -polymorphs,  $\text{Li}_2\text{O}$ ,  $\text{LiOH}$ ,  $\text{Li}_2\text{CO}_3$ ,  $\text{Li}_2\text{C}_2\text{O}_4$ ,  $\text{Li}_2\text{C}_2$ , or  $\text{Li}_2\text{O}_2$ .

All XRD patterns were Rietveld refined in order to investigate the structural features (cubic cell parameter, crystallite size, and microstrain) of LTO electrodes tested in 1m-T and LP30. This analysis discloses insight of the structural evolution of the spinel lattice and morphological features upon long-term charge/discharge cycles. The most relevant fitting results obtained for all samples are summarized in Figure 5, with solid and dashed lines representing a simple guide for the eye.

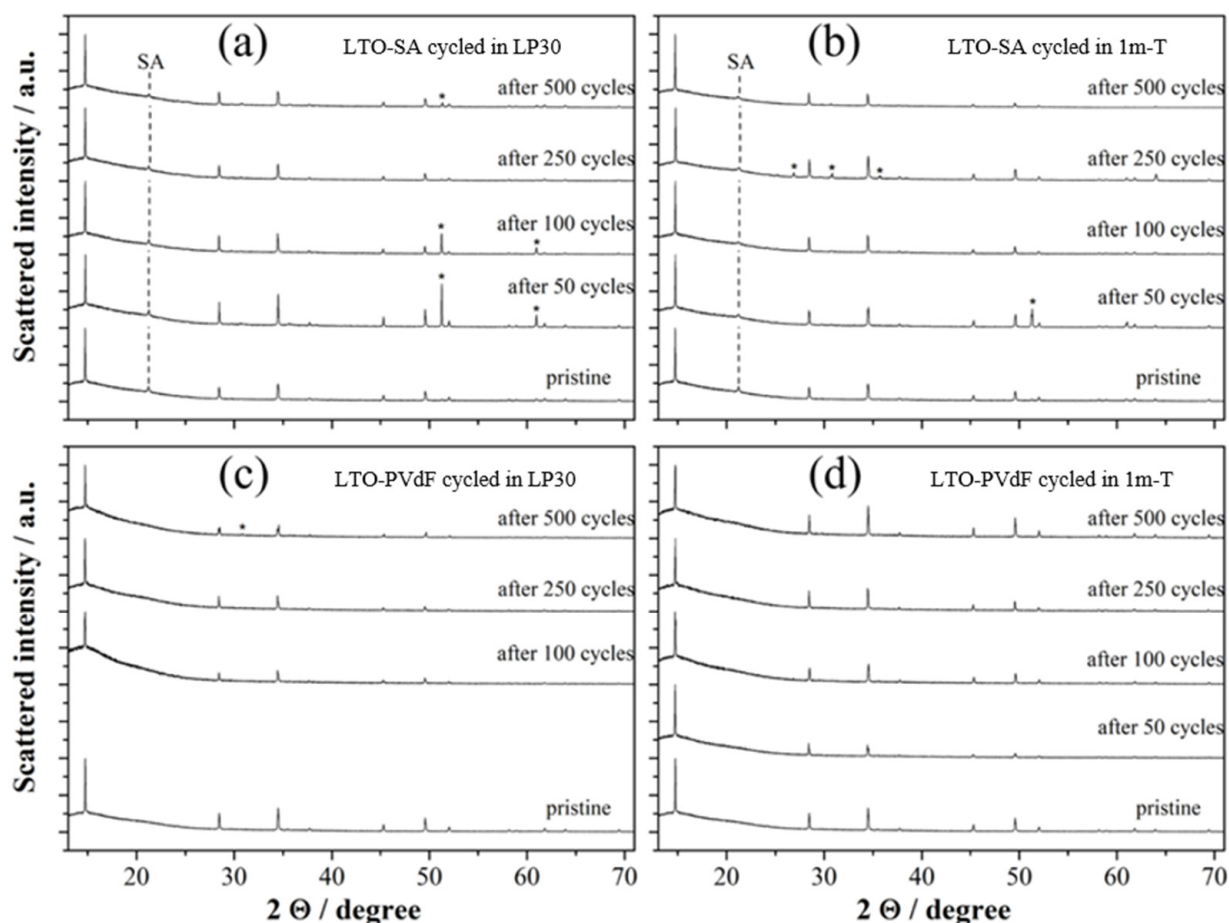


**Figure 4.** Synchrotron XRD patterns of LTO electrodes compared with pristine samples: (a) LTO-SA electrodes cycled in LP30; (b) LTO-SA electrodes cycled in 1m-T; (c) LTO-PVdF electrodes cycled in LP30; (d) LTO-PVdF electrodes cycled in 1m-T. Spurious reflection from aluminum are highlighted by asterisks.

In line with the expectation from the so-called “zero-strain” intercalation spinel, the cubic lattice parameter only marginally increases upon cycling, and the expansion in all cases is  $<0.1\%$ . This is direct evidence of the resilience of the spinel lattice toward the insertion/deinsertion of lithium ions. The slight increase in lattice parameter can be attributed to the possible accumulation of defects while cycling, and the impact of 0D, 1D, and 2D defects on the overall lattice volume of titanate spinels is well known [56,57]. The only exception is given by the LTO-PVdF electrodes cycled in the 1m-T electrolyte: in line with the rapid electrochemical deactivation, the cubic lattice remains almost unaltered upon cycling.

Regarding the morphological features derived from the Rietveld refinements, i.e., size and microstrain, all samples experience a reduction in the average dimension of the crystalline domains after cycling. Remarkably, this common trend is apparently affected by the binder employed in the manufacture of electrodes. On a related note, it is worthwhile to note that the use of SA plays a role in stabilizing the domain size upon cycling, after an initial decrease of 50% in volume. On the other hand, electrodes manufactured by the PVdF binder show a similar trend but the decrease in crystallite size occurs smoothly for approximately 250 cycles. Noticeably, the underperforming LTO-PVdF electrodes cycled in the 1m-T electrolyte show the most extensive pulverization of crystallites, and the final shrinking of D is approximately 75%.



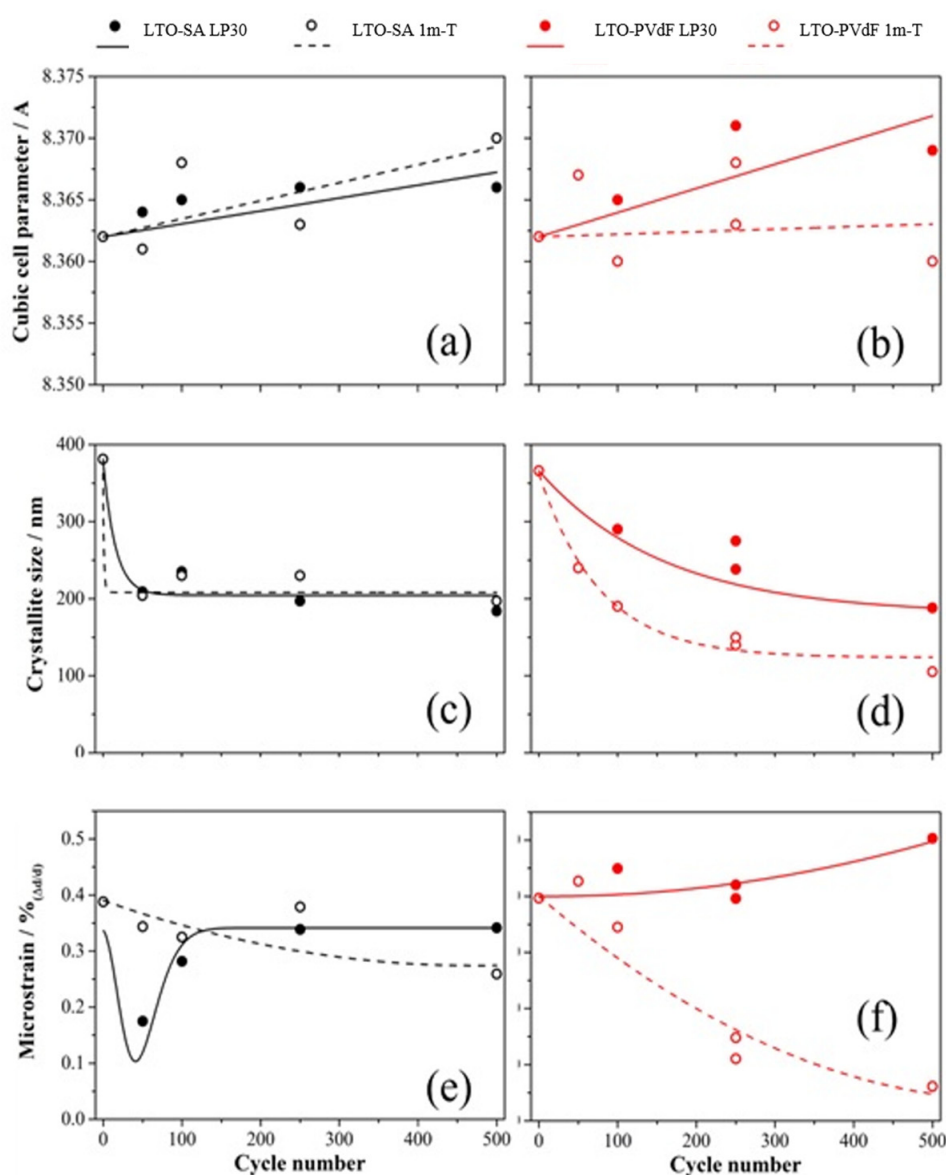


**Figure 5.** Relevant structural features (cubic cell parameter, crystallite size, and microstrain) for pristine and ex situ samples derived from the Rietveld refinements of the corresponding synchrotron XRD patterns: (a,c,e) LTO-SA (black symbol) and (b,d,f) LTO-PVdF (red symbol) electrodes tested in LP30 (full symbol) and 1m-T (empty symbol). Solid and dashed lines represent a simple guide for the eye.

Moreover, the long-range disorder does not change remarkably upon cycling, apart from the LTO-PVdF electroelectrodes cycled in the 1 m-T electrolyte for which a reduction in the microstrain is found. In the other three cases, the microstrain varies less than  $\pm 25\%$  after 500 cycles: This common trend matches nicely with the similar electrochemical performance. For the sake of completeness, the LTO-SA electrodes cycled in LP30 show a drop in the microstrain after 50 cycles, which scatters from the general trend. This evidence may be a clue of a structural rearrangement, but a clear explanation is missing, and further work is needed to clarify this point.

Overall, the XRD analysis suggests that the SA binders support an improved stability of the LTO lattice and crystallites upon cycling. In particular, in both electrolytes, the lattice parameters slightly increase by 0.1% in 500 cycles while, after an initial decrease in the crystallite size of about 50% in 50 cycles, a negligible alteration of the crystal domain size is observed in the following 450 cycles. Additionally, changes in microstrain are limited to

25% up to 500 cycles. The PVdF binder proves to be less effective in preserving the LTO lattice and crystallites, thus suggesting the possibility of a direct participation of the binder in the slight, yet irreversible, change in reactivity observed upon cycling. This is in line with our previous observations already discussed in Ref. [44].

#### 4. Conclusions

In this manuscript, we addressed the changes in structure of LTO for prolonged cycling in aprotic lithium cells at room temperature. We analyzed the effect of the electrode's composition by comparing two different binders, i.e., the water-processable sodium alginate (SA) and the conventional polyvinylidene fluoride (PVdF), and that of the electrolyte nature by testing a carbonate-based (LP30) and an ether-based aprotic (LiTFSI-tetraglyme, 1m-T) electrolyte. The study was carried out *ex situ*, using synchrotron XRD, on post-mortem electrodes collected at different stages from the cycled cells.

From the electrochemical point of view, the use of the aqueous SA binder is strongly beneficial as it allows excellent reversibility and performance for 500 cycles in both the carbonate-based LP30 electrolyte and in the ether-based 1m-T electrolyte. On the other hand, the electrodes manufactured with the PVdF binder show electrolyte-dependent performance. In both cases the initial performance is comparable (cycles 1–20 are in line with the SA binder), but in LP30, a constant capacity fading is observed in the following cycles, and in 1m-T, a rapid deactivation is recorded. These results have been confirmed in multiple tests.

Rietveld analysis suggests that the SA binder promotes the stability of the LTO lattice and crystallites upon cycling, and the evolution of the crystal lattice, the crystallite size, and the crystal microstrain are very similar in both electrolytes and are analogous to that of the LTO-PVdF electrodes cycled in LP30. Overall, the PVdF binder appears to be less effective in preserving the LTO lattice and crystallite size, thus suggesting the possibility of a direct participation of the binder in irreversible reactivity occurring upon cycling.

**Author Contributions:** Conceptualization, F.D.G., S.B. and C.A.; methodology, F.D.G., S.B. and C.A.; software, F.D.G. and S.B.; validation, M.G., L.G., S.B. and C.A.; formal analysis, F.D.G. and S.B.; investigation, F.D.G., S.B. and C.A.; resources, S.B. and C.A.; data curation, F.D.G., S.B. and C.A.; writing—original draft preparation, F.D.G. and S.B.; writing—review and editing, F.D.G., M.G., L.G., S.B. and C.A.; visualization, F.D.G. and S.B.; supervision, S.B. and C.A.; project administration, C.A.; funding acquisition, S.B. and C.A. All authors have read and agreed to the published version of the manuscript.

**Funding:** This research was funded by Ministry for Education, University and Research (MIUR)-Deutscher Akademischer Austauschdienst (DAAD) Joint Mobility Program (JMP) "Interface properties of electrode materials" (Project number 57265580). One of us (SB) would like to recognize the financial support by the Italian Minister of Economic Development (MISE) in the framework of "Ricerca di Sistema Elettrico" (grant number I34I19005780001) in close collaboration with Italian National Agency for New Technologies, Energy and Sustainable Economic Development (ENEA).

**Institutional Review Board Statement:** Not applicable.

**Informed Consent Statement:** Not applicable.

**Data Availability Statement:** Data are available at the corresponding author.

**Acknowledgments:** F.D.G., S.B., C.A. would like to acknowledge Elettra Sincrotrone Trieste (Italy) for granting beamtime to carry out the XRD experiments reported herein (proposal no. 20180238); F.D.G. and C.A. would like to acknowledge Karl-Heinz Pettinger (University of Applied Sciences Landshut) for having provided LTO powder.

**Conflicts of Interest:** The authors declare no conflict of interest. The funders had no role in the design of the study; in the collection, analyses, or interpretation of data; in the writing of the manuscript; or in the decision to publish the results.

## References

1. International Energy Agency Net Zero by 2050. A Roadmap for the Global Energy Sector. Available online: <https://www.iea.org/reports/net-zero-by-2050> (accessed on 10 March 2022).
2. On the Implementation of the Strategic Action Plan on Batteries: Building a Strategic Battery Value Chain in Europe Brussels, 9.4.2019 COM (2019) 176 Final. Available online: [https://eur-lex.europa.eu/resource.html?uri=cellar:72b1e42b-5ab2-11e9-9151-01aa75ed71a1.0001.02/DOC\\_1&format=PDF](https://eur-lex.europa.eu/resource.html?uri=cellar:72b1e42b-5ab2-11e9-9151-01aa75ed71a1.0001.02/DOC_1&format=PDF) (accessed on 7 January 2022).
3. World Economic Forum. A Vision for a Sustainable Battery Value Chain in 2030, Global Battery Alliance. Available online: [Ttps://www3.weforum.org/docs/WEF\\_A\\_Vision\\_for\\_a\\_Sustainable\\_Battery\\_Value\\_Chain\\_in\\_2030\\_Report.pdf](https://www3.weforum.org/docs/WEF_A_Vision_for_a_Sustainable_Battery_Value_Chain_in_2030_Report.pdf) (accessed on 10 March 2022).
4. Tian, Y.; Zeng, G.; Rutt, A.; Shi, T.; Kim, H.; Wang, J.; Koettgen, J.; Sun, Y.; Ouyang, B.; Chen, T.; et al. Promises and challenges of next-generation “beyond Li-ion” batteries for electric vehicles and grid decarbonization. *Chem. Rev.* **2021**, *121*, 1623–1669. [[CrossRef](#)]
5. Wu, F.; Maier, J.; Yu, Y. Guidelines and trends for next-generation rechargeable lithium and lithium-ion batteries. *Chem. Soc. Rev.* **2020**, *49*, 1569–1614. [[CrossRef](#)] [[PubMed](#)]
6. Sharma, S.S.; Manthiram, A. Towards more environmentally and socially responsible batteries. *Energy Environ. Sci.* **2020**, *13*, 4087–4097. [[CrossRef](#)]
7. Amici, J.; Asinari, P.; Ayerbe, E.; Barboux, P.; Bayle-Guillemaud, P.; Behm, R.J.; Berecibar, M.; Berg, E.; Bhowmik, A.; Bodoardo, S.; et al. A roadmap for transforming research to invent the batteries of the future designed within the european large scale research initiative BATTERY 2030+. *Adv. Energy Mater.* **2022**, *12*, 2102785–2102826. [[CrossRef](#)]
8. Kaliaperumal, M.; Dharanendrakumar, M.S.; Prasanna, S.; Abhishek, K.V.; Chidambaram, R.K.; Adams, S.; Zaghbi, K.; Reddy, M.V. Cause and mitigation of lithium-ion battery failure—A review. *Materials* **2021**, *14*, 5676. [[CrossRef](#)] [[PubMed](#)]
9. Lach, J.; Wróbel, K.; Wróbel, J.; Czerwiński, A. Applications of carbon in rechargeable electrochemical power sources: A review. *Energies* **2021**, *14*, 2649. [[CrossRef](#)]
10. Yan, H.; Zhang, D.; Qilu, D.; Duo, X.; Sheng, X. A review of spinel lithium titanate ( $\text{Li}_4\text{Ti}_5\text{O}_{12}$ ) as electrode material for advanced energy storage devices. *Ceram. Int.* **2021**, *47*, 5870–5895. [[CrossRef](#)]
11. Zhao, B.; Ran, R.; Liu, M.; Shao, Z. A comprehensive review of  $\text{Li}_4\text{Ti}_5\text{O}_{12}$ -based electrodes for lithium-ion batteries: The latest advancements and future perspectives. *Mater. Sci. Eng. R* **2015**, *98*, 1–71. [[CrossRef](#)]
12. Xu, G.; Han, P.; Dong, S.; Liu, H.; Cui, G.; Chen, L.  $\text{Li}_4\text{Ti}_5\text{O}_{12}$ -based energy conversion and storage systems: Status and prospects. *Coord. Chem. Rev.* **2017**, *343*, 139–184. [[CrossRef](#)]
13. Björklund, E.; Brandell, D.; Hahlin, M.; Edström, K.; Younesi, R. How the negative electrode influences interfacial and electrochemical properties of  $\text{LiNi}_{1/3}\text{Co}_{1/3}\text{Mn}_{1/3}\text{O}_2$  cathodes in Li-ion batteries. *J. Electrochem. Soc.* **2017**, *164*, A3054–A3059. [[CrossRef](#)]
14. Ding, Y.; Cano, Z.P.; Yu, A.; Lu, J.; Chen, Z. Automotive Li-ion batteries: Current status and future perspectives. *Electrochem. Energy Rev.* **2019**, *2*, 1–28. [[CrossRef](#)]
15. Pelegov, D.V.; Pontes, J. Main drivers of battery industry changes: Electric Vehicles—A market overview. *Batteries* **2018**, *4*, 65. [[CrossRef](#)]
16. Nemeth, T.; Schröer, P.; Kuipers, M.; Sauer, D.U. Lithium titanate oxide battery cells for high-power automotive applications—Electro-thermal properties, aging behavior and cost considerations. *J. Energy Storage* **2020**, *31*, 101656–101669. [[CrossRef](#)]
17. Takami, N.; Inagaki, H.; Tatebayashi, Y.; Saruwatari, H.; Honda, K.; Egusa, S. High-power and long-life lithium-ion batteries using lithium titanium oxide anode for automotive and stationary power applications. *J. Power Sources* **2013**, *244*, 469–475. [[CrossRef](#)]
18. Haridas, A.K.; Jyothirmayi, A.; Sharma, C.S.; Rao, T.N. Synergic effect of nanostructuring and excess  $\text{Mn}^{3+}$  content in the electrochemical performance of  $\text{Li}_4\text{Ti}_5\text{O}_{12}$ - $\text{LiNi}_{0.5}\text{Mn}_{1.5}\text{O}_4$  Li-ion full-cells. *J. Mater. Res.* **2020**, *35*, 42–50. [[CrossRef](#)]
19. Aktekin, B.; Lacey, M.J.; Nordh, T.; Younesi, R.; Tengstedt, C.; Zipprich, W.; Brandell, D.; Edström, K. Understanding the capacity loss in  $\text{LiNi}_{0.5}\text{Mn}_{1.5}\text{O}_4$ - $\text{Li}_4\text{Ti}_5\text{O}_{12}$  lithium-ion cells at ambient and elevated temperatures. *J. Phys. Chem. C* **2018**, *122*, 11234–11248. [[CrossRef](#)]
20. Wu, H.M.; Belharouak, I.; Deng, H.; Abouimrane, A.; Sun, Y.-K.; Amine, K. Development of  $\text{LiNi}_{0.5}\text{Mn}_{1.5}\text{O}_4/\text{Li}_4\text{Ti}_5\text{O}_{12}$  system with long cycle life. *J. Electrochem. Soc.* **2009**, *156*, A1047–A1050. [[CrossRef](#)]
21. Patoux, S.; Sannier, L.; Lignier, H.; Reynier, Y.; Bourbon, C.; Jouanneau, S.; Le Cras, F.; Martinet, S. High voltage nickel manganese spinel oxides for Li-ion batteries. *Electrochim. Acta* **2008**, *53*, 4137–4145. [[CrossRef](#)]
22. Nguyen, M.T.; Sutton, P.; Palumbo, A.; Fischer, M.G.; Hua, X.; Gunkel, I.; Steiner, U. Polymer-Templated Mesoporous lithium titanate microspheres for high-performance lithium batteries. *Mater. Adv.* **2022**, *3*, 362–372. [[CrossRef](#)] [[PubMed](#)]
23. Yin, Y.; Luo, X.; Xu, B. In-situ self-assembly synthesis of low-cost, long-life, shape-controllable spherical  $\text{Li}_4\text{Ti}_5\text{O}_{12}$  anode material for Li-ion batteries. *J. Alloys Compd.* **2022**, *904*, 164026–164036. [[CrossRef](#)]
24. Birrozzi, A.; Copley, M.; Von Zamory, J.; Pasqualini, M.; Calcaterra, S.; Nobili, F.; Cicco, A.D.; Rajantie, H.; Briceno, M.; Bilbé, E.; et al. Scaling up “Nano”  $\text{Li}_4\text{Ti}_5\text{O}_{12}$  for high-power lithium-ion anodes using large scale flame spray pyrolysis. *J. Electrochem. Soc.* **2015**, *162*, A2331–A2338. [[CrossRef](#)]
25. Wang, G.; Wang, H.; Ma, G.; Du, X.; Du, L.; Jing, P.; Wang, Y.; Wu, K.; Wu, H.; Wang, Q.; et al. Investigation on process mechanism of a novel energy-saving synthesis for high performance  $\text{Li}_4\text{Ti}_5\text{O}_{12}$  anode material. *J. Energy Chem.* **2022**, *70*, 266–275. [[CrossRef](#)]

26. Deng, Z.; Xu, Z.; Deng, W.; Wang, X. Ultrafine  $\text{Li}_4\text{Ti}_5\text{O}_{12}$  nanocrystals as building blocks for ultrahigh-power lithium-ion battery anodes. *J. Power Sources* **2022**, *521*, 230970. [[CrossRef](#)]
27. Bhatti, H.S.; Jabeen, S.; Mumtaz, A.; Ali, G.; Qaisar, S.; Hussain, S. Effects of cobalt doping on structural, optical, electrical and electrochemical properties of  $\text{Li}_4\text{Ti}_5\text{O}_{12}$  anode. *J. Alloys Compd.* **2022**, *890*, 161691–161703. [[CrossRef](#)]
28. Yi, T.F.; Yang, S.Y.; Xie, Y. Recent advances of  $\text{Li}_4\text{Ti}_5\text{O}_{12}$  as a promising next generation anode material for high power lithium-ion batteries. *J. Mater. Chem. A* **2015**, *3*, 5750–5777. [[CrossRef](#)]
29. Kaftelen, H.; Tuncer, M.; Tu, S.; Repp, S.; Göçmez, H.; Thomann, R.; Weber, S.; Erdem, E. Mn-substituted spinel  $\text{Li}_4\text{Ti}_5\text{O}_{12}$  materials studied by multifrequency EPR spectroscopy. *J. Mater. Chem. A* **2013**, *1*, 9973–9982. [[CrossRef](#)]
30. Capsoni, D.; Bini, M.; Massarotti, V.; Mustarelli, P.; Ferrari, S.; Chiodelli, G.; Mozzati, M.C.; Galinetto, P. Cr and Ni doping of  $\text{Li}_4\text{Ti}_5\text{O}_{12}$ : Cation distribution and functional properties. *J. Phys. Chem. C* **2009**, *113*, 19664–19671. [[CrossRef](#)]
31. Toigo, C.; Kracalik, M.; Bradt, E.; Pettinger, K.H.; Arbizzani, C. Rheological properties of aqueous SA slurries for LTO battery electrodes. *Polymers* **2021**, *13*, 3582. [[CrossRef](#)] [[PubMed](#)]
32. Toigo, C.; Arbizzani, C.; Pettinger, K.H.; Biso, M. Study on different water-based binders for  $\text{Li}_4\text{Ti}_5\text{O}_{12}$  electrodes. *Molecules* **2020**, *25*, 2443. [[CrossRef](#)]
33. Karuppiah, S.; Franger, S.; Nallathamby, K. Water-Soluble Green Binder for  $\text{Li}_4\text{Ti}_5\text{O}_{12}$  anode: Effect of binder choice on its lithium storage property. *ChemElectroChem* **2018**, *5*, 343–349. [[CrossRef](#)]
34. Bresser, D.; Buchholz, D.; Moretti, A.; Passerini, S. Alternative binders for sustainable electrochemical energy storage—The transition to aqueous electrode processing and bio-derived polymers. *Energy Environ. Sci.* **2018**, *11*, 3096–3127. [[CrossRef](#)]
35. He, M.; Castel, E.; Laumann, A.; Nuspl, G.; Novák, P.; Berg, E.J. In situ gas analysis of  $\text{Li}_4\text{Ti}_5\text{O}_{12}$  based electrodes at elevated temperatures. *J. Electrochem. Soc.* **2015**, *162*, A870–A876. [[CrossRef](#)]
36. Bernhard, R.; Meini, S.; Gasteiger, H.A. On-line electrochemical mass spectrometry investigations on the gassing behavior of  $\text{Li}_4\text{Ti}_5\text{O}_{12}$  and its origins. *J. Electrochem. Soc.* **2014**, *161*, A497–A505. [[CrossRef](#)]
37. Hoffmann, J.; Milien, M.S.; Lucht, B.L.; Payne, M. Investigation of gas evolution from  $\text{Li}_4\text{Ti}_5\text{O}_{12}$  anode for lithium-ion batteries. *J. Electrochem. Soc.* **2018**, *165*, A3108–A3113. [[CrossRef](#)]
38. Lv, W.; Gu, J.; Niu, Y.; Wen, K.; He, W. Review—Gassing mechanism and suppressing solutions in  $\text{Li}_4\text{Ti}_5\text{O}_{12}$ -based lithium-ion batteries. *J. Electrochem. Soc.* **2017**, *164*, A2213–A2224. [[CrossRef](#)]
39. Han, C.; He, Y.; Liu, M.; Li, B.; Yang, Q.-H.; Wong, C.-P.; Kang, F. A review of gassing behavior in  $\text{Li}_4\text{Ti}_5\text{O}_{12}$ -based lithium-ion batteries. *J. Mater. Chem. A* **2017**, *5*, 6368–6381. [[CrossRef](#)]
40. Liu, J.; Bian, P.; Li, J.; Ji, W.; Hao, H.; Yu, A. Gassing behavior of lithium titanate-based lithium-ion batteries with different types of electrolytes. *J. Power Sources* **2015**, *286*, 380–387. [[CrossRef](#)]
41. Govindarajan, K.; Nasara, R.N.; Lin, S.-K. Clarification on the gassing behavior of carbon-coated  $\text{Li}_4\text{Ti}_5\text{O}_{12}$  at elevated temperature: Importance of coating coverage. *Batter. Supercaps* **2022**, *6*, e202200010.
42. Milien, M.S.; Hoffmann, J.; Payne, M.; Lucht, B.L. Effect of electrolyte additives on  $\text{Li}_4\text{Ti}_5\text{O}_{12}$  cycling performance and gas evolution. *J. Electrochem. Soc.* **2018**, *165*, A3925–A3931. [[CrossRef](#)]
43. Yuan, T.; Tan, Z.; Ma, C.; Yang, J.; Ma, Z.F.; Zheng, S. Challenges of spinel LTO for lithium-ion battery industrial applications. *Adv. Energy Mater.* **2017**, *7*, 1601625–1601649. [[CrossRef](#)]
44. De Giorgio, F.; La Monaca, A.; Dinter, A.; Frankenberger, M.; Pettinger, K.H.; Arbizzani, C. Water-processable  $\text{Li}_4\text{Ti}_5\text{O}_{12}$  electrodes featuring eco-friendly sodium alginate binder. *Electrochim. Acta* **2018**, *289*, 112–119. [[CrossRef](#)]
45. Sloop, S.E.; Kerr, J.B.; Kinoshita, K. The role of Li-ion battery electrolyte reactivity in performance decline and self-discharge. *J. Power Sources* **2003**, *119*, 330–337. [[CrossRef](#)]
46. Orita, A.; Kamijima, K.; Yoshida, M.; Dokko, K.; Watanabe, M. Favorable combination of positive and negative electrode materials with glyme-Li salt complex electrolytes in lithium-ion batteries. *J. Power Sources* **2011**, *196*, 3874–3880. [[CrossRef](#)]
47. Di Lecce, D.; Marangon, V.; Jung, H.G.; Tominaga, Y.; Greenbaum, S.; Hassoun, J. Glyme-based electrolytes: Suitable solutions for next-generation lithium batteries. *Green Chem.* **2022**, *24*, 1021–1048. [[CrossRef](#)]
48. Plaisier, J.R.; Nodari, L.; Gigli, L.; Miguel, E.P.R.S.; Bertinello, R.; Lausi, A. The X-Ray diffraction beamline MCX at Elettra: A case study of non-destructive analysis on stained glass. *Acta IMEKO* **2017**, *6*, 71–75. [[CrossRef](#)]
49. Toby, B.H.; Von Dreele, R.B. GSAS-II: The Genesis of a modern open-source all-purpose crystallography software package. *J. Appl. Crystallogr.* **2013**, *46*, 544–549. [[CrossRef](#)]
50. Deschanvres, A.; Raveau, B.; Sekkal, Z. Mise en évidence et étude cristallographique d'une nouvelle solution solide de type spinelle  $\text{Li}_{1+x}\text{Ti}_{2-x}\text{O}_4$   $0 \leq x \leq 0.333$ . *Mat. Res. Bull.* **1971**, *6*, 699–704. [[CrossRef](#)]
51. Paufler, P. *The Rietveld Method*; Young, R.A., Ed.; Oxford University Press: Oxford, UK, 1995.
52. Zhang, W.; Topsakal, M.; Cama, C.; Pelliccione, C.J.; Zhao, H.; Ehrlich, S.; Wu, L.; Zhu, Y.; Frenkel, A.I.; Takeuchi, K.J.; et al. Multi-stage structural transformations in zero-strain lithium titanate unveiled by in situ X-ray absorption fingerprints. *J. Am. Chem. Soc.* **2017**, *139*, 16591–16603. [[CrossRef](#)]
53. Wagemaker, M.; Simon, D.R.; Kelder, E.M.; Schoonman, J.; Ringpfeil, C.; Haake, U.; Lützenkirchen-Hecht, D.; Frahm, R.; Mulder, F.M. A kinetic two-phase and equilibrium solid solution in spinel  $\text{Li}_{4+x}\text{Ti}_5\text{O}_{12}$ . *Adv. Mater.* **2006**, *18*, 3169–3173. [[CrossRef](#)]
54. Zhu, W.; Wang, Y.; Liu, D.; Gariépy, V.; Gagnon, C.; Vijh, A.; Trudeau, M.L.; Zaghbi, K. Application of operando X-ray diffraction in various aspects of the investigations of lithium/sodium-ion batteries. *Energies* **2018**, *11*, 2963. [[CrossRef](#)]

55. Verde, M.G.; Baggetto, L.; Balke, N.; Veith, G.M.; Seo, J.K.; Wang, Z.; Meng, Y.S. Elucidating the phase transformation of  $\text{Li}_4\text{Ti}_5\text{O}_{12}$  lithiation at the nanoscale. *ACS Nano* **2016**, *10*, 4312–4321. [[CrossRef](#)] [[PubMed](#)]
56. Tsai, P.-C.; Hsu, W.-D.; Lin, S.-K. Atomistic structure and ab initio electrochemical properties of  $\text{Li}_4\text{Ti}_5\text{O}_{12}$  defect spinel for Li ion batteries. *J. Electrochem. Soc.* **2014**, *161*, A439–A444. [[CrossRef](#)]
57. Zhang, H.; Yang, Y.; Xu, H.; Wang, L.; Lu, X.; He, X.  $\text{Li}_4\text{Ti}_5\text{O}_{12}$  spinel anode: Fundamentals and advances in rechargeable batteries. *InfoMat* **2022**, *4*, e12228. [[CrossRef](#)]